Journal Name

ARTICLE

# Sodium Difluorophosphate: Facile Synthesis, Structure, and Electrochemical Behavior as an Additive for Sodium-ion Batteries

Received 00th January 20xx,
Accepted 00th January 20xx

DOI: 10.1039/x0xx00000x

www.rsc.org/

Huan Yang, [a] Jinkwang Hwang,[a] Yuto Tonouchi,[a] Kazuhiko Matsumoto,*[,a,b] Rika Hagiwara[a,b]

Despite the success of difluorophosphate ($PO_2F_2^-$, DFP) electrolyte additives in lithium and potassium-ion batteries, their utilization in sodium-ion batteries remains unexplored due to difficulties in the synthesis of sodium difluorophosphates (NaDFP). Thus, in this study, NaDFP salt prepared via ion exchange of KDFP and $NaPF_6$ is characterized using single-crystal X-ray diffraction, Raman and infrared (IR) spectroscopy, energy dispersive X-ray analysis (EDX), and thermogravimetry-differential thermal analysis (TG-DTA). Electrochemical tests demonstrate enhanced cycle performance of a hard carbon electrode (capacity retention; 76.3% after 500 cycles with NaDFP vs. 59.2% after 200 cycles in the neat electrolyte), achieving a high Coulombic efficiency (average of 99.9% over 500 cycles) when NaDFP is used as an electrolyte additive. Further, electrochemical impedance spectroscopy (EIS) using a HC/HC symmetric cell demonstrates significant reduction of the interfacial resistance upon addition of NaDFP. X-ray photoelectron spectroscopy (XPS) indicates presence of a stable, $Na^+$-conducting solid–electrolyte interphase (SEI) components formed in presence of NaDFP. This work not only presents a feasible NaDFP synthesis method, but also demonstrates the use of NaDFP as a strategy for optimizing sodium-ion battery performance.

## Introduction

As electrolyte formulation significantly influences battery performance, their optimization remains critical to battery development.[1] Notably, incorporating additives into electrolyte compositions is considered an apt method for improving the performance of commercialized lithium-ion batteries (LIBs).[2-5] Unlike LIBs, in the absence of additives, the electrochemical measurement of sodium-ion batteries (SIBs) utilizing conventional carbonated electrolytes becomes difficult.[6-11]

Fluoroethylene carbonate (FEC), a commonly-used electrolyte additive, has been found to improve the efficiency and stability of batteries.[1, 12] However, detrimental effects emerging from FEC include the formation of a more resistive solid-electrolyte interphase (SEI) layer on hard carbon electrodes (HC), resulting in an increase in the voltage polarization; thereby culminating to attenuation in the cyclability.[12-17] Thus, a functional additive that can form an excellent SEI layer (*viz*., thin and homogenous film with high conductivity) is pivotal to the performance of SIBs. In this regard, various researches on revealing the SEI formation and interphase properties of SIBs have been conducted using a variety of salt, solvent, and additive combinations such as $NaPF_6$, $NaClO_4$, NaTFSA (Sodium bis(trifluoromethylsulfonyl)amide), NaFTA sodium (fluorosulfonyl)(trifluoromethylsulfonyl)amide), and NaFSA (sodium bis(fluorosulfonyl)amide) and EC (ethylene carbonate), DEC (diethylcarbonate), DME (Dimethoxyethane), DMC (Dimethyl carbonate), PC (Propylene carbonate) with additives of VC (vinylene carbornate) and FEC, as manipulating various concentrations and ratios.[6, 18-22]

Among the widely investigated phosphate structures, fluorophosphate salts have drawn immense attention, even more than orthophosphates, in inorganic chemistry on account of their compositional and structural diversity arising from their anion bond linkage wherein fluorine atoms are more covalently bound to the phosphorus atom.[23-31] In particular, difluorophosphate (DFP) salts, which are intermediate decomposition products of $MPF_6$ (M = Li, or K),[32-35] in hydrolysis, have been investigated as electrolyte components (salt and additive) not only for LIBs but also for potassium-ion batteries (PIBs).[36-38] As electrolyte additives, difluorophosphate salts have been found to facilitate the formation of ionically conductive SEI layers, which significantly improve the electrochemical performance of batteries. In previous studies, electrolytes containing LiDFP and KDFP additives were found to form SEI layers comprising $PO_x$ species, which improved interfacial properties and reduced the overpotential of graphite electrodes during cycling.[39-43] Despite their efficacy in LIBs and PIBs systems, this class of materials remains underexplored in SIBs.

Despite the auspicious prospects, the synthesis of pure difluorophosphate salts presents a major challenge to their

[a] Graduate School of Energy Science, Kyoto University, Sakyo-ku, Kyoto 606-8501, Japan
[b] Unit of Elements Strategy Initiative for Catalysts & Batteries (ESICB), Kyoto University, Katsura, Kyoto 615-8510, Japan

*Corresponding author: Kazuhiko Matsumoto
E-mail: k-matsumoto@energy.kyoto-u.ac.jp
Tel: +81757534817
Fax: +81757535906

† Electronic supplementary information (ESI) available: See DOI: 10.XXXXXXX

advancement. Although difluorophosphates can be prepared using $HPO_2F_2$, its anhydrous form ($P_2O_3F_4$), or $HPF_6$, the corrosive nature of these precursor materials considerably impedes their practicality.[44-47] Other synthetic routes also involve intricate steps, whereas lab-scale syntheses are often contentious.

Herein, we report a facile and scalable two-step synthesis of sodium difluorophosphate (NaDFP) additive. The crystal structure was ascertained, enabling us to complete the chemical row series of major monovalent DFP salts ($Li^+$, $K^+$, $Rb^+$, $Cs^+$, $NH_4^+$, and $Ag^+$).[46-51] The thermal and spectroscopic properties of NaDFP were examined by thermogravimetric and differential thermal analysis (TG-DTA), Raman and infrared (IR) spectroscopy. The influence of the NaDFP additive on the Na metal deposition-dissolution behavior and electrochemical performance of hard carbon (HC) electrodes is investigated in detail, and a comparison with the well-known FEC and neat electrolyte (electrolyte without additives) was drawn using symmetric cell electrochemical impedance spectroscopy (EIS), and X-ray photoelectron spectroscopy (XPS).

## Experimental

### Apparatus and Materials

Volatile materials were handled in a vacuum line made from stainless steel, Pyrex glass, and PFA (tetrafluoroethylene-perfluoroalkylvinylether copolymer). Non-volatile materials were handled under a dry argon atmosphere in a glove box or a dry air atmosphere in a dry chamber. The starting salts, $KPO_3$ (Aldrich, purity > 99%), $KPF_6$ (Aldrich, purity > 99%), and $NaPF_6$ (Tokyo Chemical Industry, purity > 99%), were dried under vacuum for 24 h at 353 K before use. A precursor KDFP was synthesized through the reaction of $KPO_3$ and $KPF_6$ in the molar ratio of 2:1 by heating the starting materials at 593 K in a platinum crucible over three days.[33] Tetrahydrofuran (THF; Wako, water content < 10 ppm, oxygen content < 1 ppm) was used as-purchased. The [1-ethyl-3-methylimidazoliulm][bis(fluorosulfonyl)amide] ionic liquid (Kanto Chemical, purity > 99.9%, water content < 30 ppm) was dried under vacuum for 24 h at 353 K.

### Synthesis of NaDFP

The difluorophosphate salt, NaDFP, was synthesized by a metathesis reaction in a molar ratio of KDFP : $NaPF_6$ = 1 : 1.2. $NaPF_6$ (Tokyo Chemical Industry, purity > 99%) and the as-prepared KDFP were added into dehydrated tetrahydrofuran (approximately 200 $cm^3$ in a conical flask). After agitation for 48 h using a magnetic stirrer at room temperature under airtight conditions, the solid precipitate was isolated by centrifuging the mixture. The collected precipitate was washed with THF (approximately 200 $cm^3$ in a conical flask) by stirring for 24 h in the dry chamber twice. Repetitive recrystallization in THF from 353 K to 273 K was performed when the precipitate obtained from the reaction was a fine powder, to grow larger crystals for ease of handling. The final product was dried under vacuum for 24 h at 353 K prior to use. The absence of the residual $KPF_6$, KDFP, and $NaPF_6$ in the product was confirmed by vibrational spectroscopy and energy dispersive X-ray spectroscopy (EDX) (see below).

### Characterization

Single crystals of NaDFP were grown by slowly cooling NaDFP-saturated [1-ethyl-3-methylimidazoliulm] [bis(fluorosulfonyl) amide] ionic liquid from 363 K to room temperature. Single-crystal X-ray diffraction measurements were performed using an R-axis Rapid II diffractometer (Rigaku Corporation) controlled by RAPID AUTO 2.40 software. The selected crystal was fixed in a sealed quartz capillary under a dry air atmosphere and mounted on the diffractometer under a cold dry-nitrogen flow. Data collection was performed at 113 K and consisted of 12 ω scans (130–190°, 5° per frame) at fixed ϕ (0°) and χ (45°) angles and 32 ω scans (0–160°, 5° per frame) at fixed ϕ (180°) and χ(45°) angles. The X-ray output was 50 kV–40 mA, and the exposure time was 1000 s $deg^{-1}$. Integration, scaling and absorption corrections were performed using RAPID AUTO 2.40 software. The structure was solved using SIR-92[52] and refined by SHELXL-2018/3[53] linked to Win-GX.[54] Anisotropic displacement factors were introduced for all the atoms. Full crystallographic data was curated in the joint CCDC/Fiz Karlsruhe Crystal Structure Database under CSD-2047480.

Raman spectra were recorded by a DXR3 Smart Raman spectrometer (Thermo Fisher Scientific) using a 532 nm diode-pumped solid-state laser. The sample used for Raman spectroscopy was sealed in a glass cell and isolated from the air. Infrared spectra were recorded by an ALPHA II Fourier transform IR spectrometer (ALPHA II, Bruker Optics Laboratories, Inc.) equipped with an attenuated total reflection (ATR) module under the dry air atmosphere. Morphology of NaDFP was observed via scanning electron microscopy (SEM) (Hitachi SU-8020), and EDX mapping was obtained using an EMAXEvolution X-max analyser (Horiba) attached to the SEM machine. The thermal stability was measured by TG-DTA analysis (Rigaku Thermo Plus EVO II TG 8120) at a scan rate of 5 K $min^{-1}$ under a dry Ar atmosphere. Samples were loaded on Al pans. The ionic conductivities were measured using the EIS technique. The samples for the ionic conductivity measurements were sealed into an airtight T-shaped cell equipped with stainless steel disk electrodes in a dry Ar atmosphere. The cell was placed in a thermostatic chamber (SU-241, ESPEC).

### Electrolytes and electrodes preparation

NaDFP powder was added into 1 M $NaPF_6$-ethylene carbonate and dimethyl carbonate (EC/DMC, in a 1:1 volume ratio, Kishida Chemical Co., Ltd., > 99.0 % purity, water content < 10 ppm) and stirred for one day until reaching uniformity. Saturation of NaDFP in 1 M $NaPF_6$-EC/DMC was found to occur when the concentration of NaDFP exceeds 1 wt% (0.08 mol $kg^{-1}$). The composite electrode of HC was prepared from HC powder (Carbotron P, Kureha Battery Materials Japan Co., Ltd), AB, and PVDF (85:10:5 in wt%) by uniformly mixing them in NMP

 

(solid/liquid ratio of 0.50). The obtained slurry was coated onto an Al foil and vacuum-dried at 333 K. 10 mm diameter electrodes were punched out from the foil and were vacuum-dried at 333 K for 10 h prior to cell assembly. The typical loading mass of the electrode was 2 mg $cm^{-2}$.

**Electrochemical measurement**

The electrochemical characterization of the HC electrode was carried out at 298 K using a 2032-type coin cell fabricated with the Na metal counter electrode and a glass fibre separator. For the Na/HC cell, rate capability was tested at constant current rates of 20–500 mA $(g\text{-}HC)^{-1}$ in the voltage range of 0.005–1.5 V. The cycle tests were performed at a constant current density of 100 mA $(g\text{-}HC)^{-1}$ in the same voltage range with the rate capability test. The symmetric HC/HC cells for EIS tests were assembled with the HC electrodes after 1, 3, 10, and 20 cycles in the Na/HC half cell with the selected electrolytes (at the 80% SOC). The EIS measurements were performed using a VSP potentiostat (Bio-Logic) at 298 K over a frequency range from 1 or 100 mHz to 100 kHz with an ac amplitude of 10 mV. The SEI layer components were analysed using *ex-situ* XPS (JEOL, JPS-9030, Mg *K*α source). After 20 cycles, the electrodes were washed with EC/DMC and dried at 298 K under vacuum overnight for XPS measurements.

## Results and Discussion

The NaDFP was prepared via a two-step process, as highlighted in Eqs. 1 and 2 below:

$$2KPO_3 + KPF_6 \rightarrow 3KPO_2F_2 \quad (1)$$

$$KPO_2F_2 + NaPF_6 \rightarrow NaPO_2F_2 + KPF_6 \quad (2)$$

A KDFP salt is prepared via the reaction in Eq. 1 under vacuum in a sealed container.[33, 55] Although this is a common synthesis method for KDFP, a complete reaction cannot be attained using Na analogues. As such, an ion-exchange reaction (eq. 2) was employed using the obtained KDFP and $NaPF_6$ in THF. The NADFP is collected as a precipitate due to its low solubility in THF and washed for purification. EDX mapping conducted on the material reveals an even distribution of constituent elements similar to the theoretical composition of NaDFP with no detection of residual K from the precursors. (See Fig. S1† and the brief comments in ESI†) (powder XRD pattern is also shown in Fig S1g). These results suggest that a high purity NaDFP can be obtained through a facile and scalable two-step reaction.

Further characterization was conducted using XRD to obtain crystallographic data and geometrical parameters as listed in Tables S1†, S2†, and S3†. The molecular structure of the DFP anion in NaDFP is found to have a $C_{2v}$ symmetry and it was indexed to the *P*–1 triclinic space group. This is different from other alkali metal analogues, *viz.,* KDFP, RbDFP, and CsDFP, which are isostructural species, indexable to the *Pnma* orthorhombic space group[47-49] and LiDFP indexable to the *C*2/*c* monoclinic space group (Fig. 1). Molecular geometry rendered from the crystallographic data displays no sign of disordering in the $PO_2F_2^-$ anion. Two crystallographically independent DFP ions were found to reside in each unit cell where the length of P–F bonds (1.548(2), 1.557(2), 1.562(3), and 1.555(2) Å) are longer than the P–O bond lengths (1.466(3), 1.471(3), 1.466(3), and 1.467(3) Å), similar to other alkali metal DFP salts.[47-49]. The angles of the O–P–O (121.38(16) and 121.87(16)°) bonds are found to be larger than the F–P–F angles (97.54(13) and 96.89(13)°) as a result of strong repulsion between two P=O double bonds, in concordance with the VSEPR theory.[56, 57] The Na1 atom is coordinated with five O atoms in a square pyramidal fashion (Na···O distances of 2.316(3)–2.400(3) Å), and has a secondary contact with an F atom (Na···F distance of 2.847(3) Å) at the base of the square pyramid (Fig. 1b). The Na2 coordination environment is a distorted octahedron with two F atoms (2.370(3) and 2.375(3) Å) and four O atoms (2.303(3)–2.364(3) Å), whereby the two fluorine atoms are arrayed in a *cis* position, similar to those in KDFP, RbDFP, and CsDFP (Fig. 1c).[48, 49] On the other hand, Li atoms in LiDFP coordinates with four O atoms in a tetrahedral fashion due to the smaller ionic radius of $Li^+$ compared to $Na^+$ in NaDFP.

For insights into the NaDFP bond framework, Raman and IR spectra were obtained as displayed in Fig. 1d and 1e, respectively. Table S4† summarizes the assignments of vibrational modes ($\nu$).[33] As illustrated (Fig. 1d), the main bands of the as-prepared NaDFP observed at 1304, 1140, 852, and 818 $cm^{-1}$, are assigned to four modes: $\nu_{as}(PO_2)$, $\nu_s(PO_2)$, $\nu_{as}(PF_2)$, and $\nu_s(PF_2)$ + small $\delta_s(PO_2)$, respectively (Table S4†). The three modes (*i.e.*, $\delta_s(PF_2) - \delta_s(PO_2)$, $\rho_r(PF_2) - \rho_w(PO_2)$, and $\rho_w(PF_2) - \rho_r(PO_2)$) are indistinguishable and are assigned to the two bands observed at 520 and 502 $cm^{-1}$. The $\delta_s(PF_2) - \delta_s(PO_2)$ and $\rho_t(PF_2) - \rho_t(PO_2)$ modes also overlap and are assigned to the 354 $cm^{-1}$ band. In the IR spectra (Fig. 1e), four main bands are observed. The bands at 1305 $cm^{-1}$ (shoulder at 1330 $cm^{-1}$) and 1146 $cm^{-1}$ (shoulder at 1159 $cm^{-1}$) are assigned to $\nu_{as}(PO_2)$ and $\nu_s(PO_2)$ modes, respectively whereas the absorption bands at 863 $cm^{-1}$ (shoulder at 889 $cm^{-1}$) and 863 $cm^{-1}$ are assigned to $\nu_{as}(PF_2)$ and $\nu_s(PF_2)$ + small $\delta_s(PO_2)$. The strong absorption band in the lower frequency region (498.9 $cm^{-1}$) is based on the combination modes, including scissoring, rocking and wagging modes ($\delta_s(PF_2) - \delta_s(PO_2)$, $\rho_r(PF_2) - \rho_w(PO_2)$, and $\rho_w(PF_2) - \rho_r(PO_2)$).

To ascertain the thermal stability of the prepared NaDFP, TG-DTA was conducted under an Ar atmosphere. On the TG curve (Fig. S2†), a gradual weight-loss ascribed to the hygroscopic nature of NaDFP is noted as temperatures rose from room temperature to 453 K. In the DTA curve, a two-stage weight-loss trend attributed to the decomposition of NaDFP between 453–800 K, is manifested at two points corresponding to the endothermic peaks at around 507 and 584 K (equivalent to a weight loss of ca. 50%). The weight-loss process slows down around 800 K. These observations suggest the occurrence of either one of two decomposition reactions (Eqs. 3 and 4) previously postulated for DFP salts.[51, 58]

$$2NaPO_2F_2 \rightarrow Na_2PO_3F + POF_3\uparrow \quad (3)$$

theoretical weight loss = 46.2 wt%

$$4NaPO_2F_2 \rightarrow Na_4P_2O_7 + PF_5 \uparrow + POF_3\uparrow \quad (4)$$

theoretical weight loss = 51.1 wt%

Theoretical weight loss computed from the proposed decomposition paths match the experimental weight loss.

To discern the influence of additives on the sodium metal deposition-dissolution behavior of the $NaPF_6$-based electrolyte, cyclic voltammetry was performed on half cells with Na and Al electrodes in neat electrolyte and electrolytes containing varying amounts of NaDFP and FEC additives. As shown in Fig. S3†, the cathodic and anodic currents corresponding to Na metal deposition and dissolution are observed at 0 V vs. $Na^+$/Na on the Al electrode. Coulombic efficiency corresponding to Na metal deposition/dissolution increases with the addition of NaDFP additives from 13.3% (neat electrolyte) to 21.5 % and 26.7 % in electrolytes with 0.5 wt% and 1 wt% NaDFP, respectively. NaDFP is also found to yield significantly higher Coulombic efficiency than electrolytes with 0.5 wt% and 3 wt% FEC, which attained 7.1 % and 15.2 %, respectively.

The cycling performance of Na/Na symmetric cells was tested to ascertain the voltage polarization (overpotential) arising from Na metal deposition and dissolution in the $NaPF_6$-based electrolytes containing varying amounts of NaDFP or FEC additives. Na/Na symmetric cells are employed to eliminate any influence of positive/negative electrodes.[59, 60] The symmetric cells were sequentially cycled at constant current densities of 10, 50, 100, 500, and 1000 μA $cm^{-2}$ (10 cycles for each current density) as shown in Fig. S4†. In each cycle, deposition/dissolution occurred for 8 minutes with a 2-minute rest between each step. Across all electrolytes, overpotential is observed to increase as the current density increases. In the neat electrolyte, overpotential rises from 3.8 mV (average value of 10 cycles) at 10 μA $cm^{-2}$ to 211 mV at 1000 μA $cm^{-2}$ (Fig. S4a†). The overpotential gradually decreases and became more stable with increasing concentrations of NaDFP additive; yielding 175 mV from 0.5 wt% and 122 mV from 1 wt% cycled at 1000 μA $cm^{-2}$. In contrast, in the electrolytes with FEC additives (0.5 and 3 wt% FEC), polarization was observed to be even greater than in the neat electrolytes, indicating that these systems had high interfacial resistances (Fig. S4d and S4e†). Considering the similar ionic conductivities of these electrolytes and therefore comparable bulk resistances of the test cells (Fig. S5†, See Table S5† for the ionic conductivity and the fitting parameters), the low polarization observed in the NaDFP electrolyte systems implies reduced interfacial resistance that enables facile ion kinetics and charge transfer through the SEI layers.[60, 61]

For deeper insight into the deposition/dissolution behaviour in the selected electrolyte systems, long-term deposition/dissolution tests and EIS analyses were performed on Na/Na symmetric cells cycled at a current density of 1 mA $cm^{-2}$ (30 minutes per cycle). The resulting voltage profiles and Nyquist plots are shown in Fig. 2. In the neat electrolyte, polarization increases after 20 cycles, reaching 0.3 V. The measurements were limited by a short circuit occurring after a few cycles (Fig. 2a). On the other hand, stable cycling performance is observed during cycling in NaDFP electrolyte systems. The 0.5 wt% NaDFP electrolyte system (Fig. 2c) displays a constant overpotential of 0.1 V for 50 h (100 cycles), which increases gradually thereafter until 200 h (400 cycles). The 1 wt% NaDFP system (Fig. 2e) exhibits a more stable cycling performance as it maintained the overpotential at 0.1V 200 h (400 cycles). The resistance is noted to decrease (smaller than in neat electrolyte) with increased amounts of NaDFP (Fig. 2c and 2e) and remains stable for 200h (1 wt% NaDFP), conforming to the stable polarization previously observed at varying current densities (Fig. S4†).

In the Nyquist plots taken at selected intervals, an arc with notable compressions in the high-frequency regions are observed in all electrolyte systems (Fig. 2b, 2d and 2f). In the neat electrolyte (Fig. 2b), the corresponding interfacial resistances are seen to increase with continued cycling, indicating severe decomposition occurring during Na metal deposition-dissolution.[62] On the other hand, in the NaDFP electrolyte systems, the arc become smaller and more stable with increased amounts of NaDFP, indicating stable interfacial behavior during long-term deposition/dissolution tests (Fig. 2d and 2f). The EIS measurements for the FEC electrolyte systems were terminated by a short circuit occurring after a few cycles wherein higher interfacial resistances are detected with progressive cycling, indicating relatively unstable deposition-dissolution behavior (Fig. S6†).

The influence of additives on the $Na^+$ insertion/extraction into/from HC negative electrodes was investigated using Na/HC cells comprising 1 M $NaPF_6$-EC/DMC electrolyte with 0 wt% NaDFP(neat), 0.5 wt% NaDFP, and 1 wt% NaDFP. The first and second charge-discharge curves measured at a current density of 25 mA $g^{-1}$ and the corresponding d$Q$/d$V$ plots are shown in Fig. 3. For comparison, electrolytes with 0.5 % and 3.0 % FEC were tested (Fig. S7†). The first cycle capacity and Coulombic efficiencies of the HC electrodes are listed in Table S6†. Relatively similar initial charge and discharge capacities of 342-344 mAh $g^{-1}$ and 256-260 mAh $g^{-1}$, respectively, are obtained from all electrolyte systems along with Coulombic efficiencies of 74.6 − 76.1 %. The plateaus appearing below 0.1 V and the slopes in the 0.1 to 1.2 V regions of the discharge curves are attributed to $Na^+$ insertion/extraction in nanopores and between graphene layers in HC, respectively, as reported by previous works.[63]

In the d$Q$/d$V$ plots, two SEI formation peaks are seen in all electrolyte systems (Figs. 3d-f and Figs. S7c-d). In the neat electrolyte, the two peaks appear at 1.00 and 0.52 V (Fig. 3d). Both peaks are observed to shift towards lower voltages with increasing amounts of NaDFP, appearing at 0.89 and 0.51 V in the 0.5 wt% NaDFP system and 0.81 and 0.50 V in the 1 wt% NaDFP system (Fig. 3e and 3f). However, the peaks shift to higher voltages with increasing amounts of FEC additives, where the peaks appeared at 1.11 and 0.66 V in the 0.5 wt% FEC system and 1.16 and 0.76 V in the 3.0 wt% FEC system. The differences in reduction potential peaks indicate that the composition of SEI layers formed depends on the choice of additive, indicating that the additives facilitated different SEI formation mechanisms.

Moreover, in the FEC systems, overpotentials are noted to increase with increased FEC amounts during charge and

 

discharge (Fig. S7a,b inset†), corroborating previous reports on HC electrodes.[16] Compared to the NaDFP systems, overpotential was much higher in the presence of FEC, indicative that the SEI formed in the FEC systems had lower conductivities than those in the neat or NaDFP systems. This is further affirmed by a previous study which reported high resistance values from SEI formed in electrolytes with FEC. [14] Previous works have also reported inferior rate performance in SIBs utilizing FEC. Thus, the cycle test was conducted at a relatively low rate *i.e.*, C/10.[1, 12, 16, 64]

The rate performance of the Na/HC half-cell was further assessed in the voltage range of 0.005–1.5 V under varying current densities in the sequence of 25, 50, 100, 250, 500, and 25 mA $g^{-1}$ (three cycles for each current density) as shown in Fig. 4. At the current density of 250 mA $g^{-1}$, the rate capability significantly improves from 93 mAh $g^{-1}$ in the neat electrolyte to 165 and 178 mAh $g^{-1}$ upon addition of 0.5 wt% and 1 wt% NaDFP, respectively. On the other hand, the FEC systems achieve considerably low reversible capacities at high rates. At 250 mA $g^{-1}$, only capacities of 75 and 70 mAh $g^{-1}$ are retained by the 0.5 and 3 wt% FEC systems, respectively.[16]

Figure 5 shows the cycle performance of the Na/HC cell in 1 M $NaPF_6$-EC/DMC with and without NaDFP or FEC additives. The neat electrolyte attains a capacity retention of 59.2% (200th cycle vs. 1st cycle), with progressive deterioration noted after the 200$^{th}$ cycle. In the NaDFP systems, a stable cycle performance is realized whereby capacity retentions of 61.8 and 76.3% (500th cycles vs. 1st cycle) are achieved by 0.5 and 1 wt% NaDFP systems, respectively, along with high average Coulombic efficiencies of 99.9%. Conversely, the FEC systems exhibit poor capacity retention (lower than NaDFP systems) characterized by discharge capacity fluctuations during cycling. Although stable cycle performance was realized after a few cycles (around 100 mAh $g^{-1}$), only a minimal improvement was noted in comparison with the neat electrolyte system. This deterioration on Na insertion-extraction capability of HC with the neat and with FEC-containing electrolytes is clearly observed by the corresponding charge-discharge curves and d$Q$/d$V$ plots (Fig. S8a,d,e,f,i,j). However, a stable charge-discharge behavior maintaining a long plateau with small polarization are achieved with the aid of 0.5 wt% and 1wt% NaDFP (Fig. S8b,c,g,h). The shape of charge-discharge curves and the peak positions of d$Q$/d$V$ plots barely change even after 500 cycles with NaDFP, which indicates that the SEI layer formed during early cycles are maintained until the end of cycle test.

To assess the electrochemical performance of an electrode in batteries, EIS is generally performed on symmetric cells.[61, 65, 66] Thus, EIS was conducted on HC/HC symmetric cells in 1 M $NaPF_6$-EC/DMC with and without NaDFP or FEC additive after the 1$^{st}$, 3$^{rd}$, 10$^{th}$, and 20$^{th}$ cycles at a current density of 100 mA $g^{-1}$, as shown by the Nyquist plots in Fig. 6. As illustrated by the schematic (Fig. 6f), the Nyquist plots of all the symmetric cells consist of two arcs and an oblique line corresponding to the diffusion process. The acr in the high-frequency range, denoted as $R_h$, represents either the resistance of the SEI layer or resistance factored between an electrode and current collector.[61, 67-70] The arc in the low-frequency range, denoted as $R_{ct}$, is ascribed to the charge transfer resistance. Since the $R_{ct}$ changes, depending on the SOC of each electrode, the SOC of each electrode in the HC/HC symmetric cells was fixed at 80% after cycling.[71, 72] In the Nyquist plots of the neat electrolyte (Fig. 6a), both arcs significantly expand in size with continued cycling, signifying an increase in $R_h$ and $R_{ct}$. During cycling in the NaDFP electrolyte systems, both arcs are noted to become smaller (indicating lower $R_h$ and $R_{ct}$) and more stable with increasing amounts of NaDFP (Figs. 6b-c), indicative that NaDFP facilitates the formation of robust SEI layers with lower interfacial resistance during cycling. In contrast, the addition of FEC results in higher $R_h$ and $R_{ct}$ (Figs. 6d-e). In particular, $R_{ct}$ is found to grow more significantly, reaching approximately three times the size of the $R_{ct}$ for the neat electrolyte after 20 cycles when 3 wt% FEC was used. These results demonstrate that the use of NaDFP additives is an effective strategy for reducing interfacial resistance and improving cycle performance in SIBs.

For further insight into the surface properties of the SEI formed on the HC electrodes, SEM analyses were performed on the HC electrodes before and after cycling in the 1 M $NaPF_6$-EC/DMC electrolyte with and without NaDFP or FEC. The SEM images of the pristine HC electrode are furnished alongside images of the HC electrodes after 3 cycles and 20 cycles in Figs. S8† and S9†, respectively. The pristine HC particles appear to be irregularly shaped with sharp edges.[73] After 3 cycles in the neat electrolyte (Fig. S9b†), the smooth and flat surfaces of the HC particles become rugged due to the emergence of large quantities of deposits on the surface. After 20 cycles (Fig. S10b†), the HC particles become entirely covered with surface deposits. This corresponds to the continuous formation of the SEI layer and is not only consistent with other SEM images throughout the cycles but also corroborates previous reports on HC electrode morphological evolution during cycling.[74] In the NaDFP systems (Figs. S9c-d† and S10c-d†), the smooth surfaces and sharp edges seen in the pristine electrode are preserved even after 20 cycles, indicating that NaDFP facilitates the formation of an SEI layer with remarkable properties. After 3 and 20 cycles in the FEC system (Figs. S9e-f† and Figs. S10e-f†), moderate amounts of surface deposits are seen on the HC with continued cycling. The SEM results of the HC electrodes after 500 cycles with 1wt% NaDFP indicated that smooth surface and sharp edges in the pristine electrode is still preserved even after 500 cycles (Figure S11†). This appears to be the distinguishing feature between HC electrodes in FEC and NaDFP systems that would result in the unstable cycle performance and low capacity retention seen in FEC systems.

XPS analyses were performed to ascertain the components of the SEI layer formed on the HC electrode after cycling in the electrolytes with and without NaDFP or FEC additives. XPS spectra of the electrodes after 20 cycles are shown in Fig. 7. A summary of the peak assignments and elemental quantification is furnished in Tables S8† and S9†. The main differences in the SEI composition of the electrodes cycled in the different electrolyte systems appear in the F 1s, O 1s and P 2p spectra. In the F 1s spectra, the peak appearing around 684 eV is assigned to NaF, a key component of SEI layers formed on the surface of HC electrodes.[1, 74-76] The F 1s spectra results further reveal that higher amounts of NaF are present on the SEI formed by NaDFP

(Fig. 7a, d). In the O 1s spectra, peaks corresponding to C-O and C=O bonds appear at 533.2 and 531.6 eV, respectively (Fig. 7b, d). These peaks are observed in all electrolytes, suggesting that the SEI components are products of carbonate solvent decomposition. In the O 1s spectrum of NaDFP, a peak corresponding to P-O appears at 530.7 eV.[77] In the P 1s spectra, the intensity of the peaks corresponding to P-O bond is found to be significantly higher in the presence of additives, with the largest peak appearing in the NaDFP system (Fig. 7c, d). This is attributed to the decomposition of the DFP anion, which facilitates the formation of a more conductive SEI layer on the surface of HC electrodes.[38, 42] Moreover, XPS peaks after 500 cycles with 1% NaDFP suggested that the contribution of P-O bonds in O 1s and P 2p became larger after 500 cycles compared to those after 20 cycles, indicative of robust SEI formation by NaDFP on HC during cycle.

## Conclusions

Herein, a NaDFP additive for SIBs is prepared via a two-step reaction process and further characterized using single-crystal XRD, Raman and IR spectroscopy, and TG-DTA analysis. The molecular structure of the DFP anion in NaDFP is found to have a $C_{2v}$ symmetry. The two crystallographically independent $Na^+$ ions have different coordination environments. Na1 is in a square pyramidal oxygen coordination in contact with one secondary fluorine, while Na2 is in a distorted octahedral coordination with four oxygen and two fluorine atoms arrayed in a *cis* position. The prepared NaDFP was used as an additive for SIBs. The Na metal deposition/dissolution efficiency of a $NaPF_6$-based electrolyte was found to improve with increasing concentrations of NaDFP. Improved electrochemical performance of a Na/HC cell confirmed the beneficial role of NaDFP on the formation of the SEI layer, which suppressed overpotential and interfacial resistance, as further affirmed by the EIS measurements. As a result, a high rate capability and long cycle life with capacity retentions of 76.3% over 500 cycles were achieved with 1 wt% NaDFP. SEM results confirm that electrolytes with NaDFP form a more stable SEI layer than neat electrolytes, thus mitigating further electrolyte degradation. XPS analyses reveal the presence of components attributed to additive decomposition, evincing the active participation of NaDFP in the formation of a stable SEI layer with higher ionic conductivity.

This work not only presents an easy and scalable synthesis route for a SIB electrolyte additive, it also demonstrates the active role of NaDFP on the improvement of SIB performance through the formation of an SEI layer with excellent features, paving the way for further exploration of electrolyte optimization as a viable approach for improving SIB performance.

## Conflicts of interest

There are no conflicts to declare.

## Acknowledgements

This study was partly supported by the Japanese Ministry of Education, Culture, Sports, Science and Technology (MEXT) program "Elements Strategy Initiative to Form Core Research Center" (JPMXP0112101003) and Japan Society for the Promotion of Science (JSPS, KAKENHI Grant Number 19H04695). One of the authors, H.Y., thanks to the China Scholarship Council (CSC) for the financial support.

## ORCID

Huan Yang: 0000-0002-8757-5733
Jinkwang Hwang: 0000-0003-4800-3158
Kazuhiko Matsumoto: 0000-0002-0770-9210
Rika Hagiwara: 0000-0002-7234-3980

## References

1 J. Fondard, E. Irisarri, C. Courrèges, M. R. Palacín, A. Ponrouch and R. Dedryvère, *J. Electrochem. Soc.*, 2020, **167**, 070526.
2 S. Mai, M. Xu, X. Liao, J. Hu, H. Lin, L. Xing, Y. Liao, X. Li and W. Li, *Electrochim. Acta*, 2014, **147**, 565-571.
3 J. Self, D. S. Hall, L. Madec and J. Dahn, *J. Power Sources*, 2015, **298**, 369-378.
4 X. Zuo, M. Zhao, X. Ma, X. Xiao, J. Liu and J. Nan, *Electrochim. Acta*, 2017, **245**, 705-714.
5 H. Zhang, W. Feng, J. Nie and Z. Zhou, *J. Fluorine Chem.*, 2015, **174**, 49-61.
6 A. Ponrouch, D. Monti, A. Boschin, B. Steen, P. Johansson and M. R. Palacín, *J. Mater. Chem. A*, 2015, **3**, 22-42.
7 R. Mogensen, D. Brandell and R. Younesi, *ACS Energy Lett.*, 2016, **1**, 1173-1178.
8 K. Matsumoto, J. Hwang, S. Kaushik, C.-Y. Chen and R. Hagiwara, *Energy Environ. Sci.*, 2019, **12**, 3247-3287.
9 G. Åvall, J. Mindemark, D. Brandell and P. Johansson, *Adv. Energy Mater.*, 2018, **8**, 1703036.
10 K. Kuratani, N. Uemura, H. Senoh, H. T. Takeshita and T. Kiyobayashi, *J. Power Sources*, 2013, **223**, 175-182.
11 K. Mishra, N. Yadav and S. A. Hashmi, *J. Mater. Chem. A*, 2020, **8**, 22507-22543.
12 S. Komaba, T. Ishikawa, N. Yabuuchi, W. Murata, A. Ito and Y. Ohsawa, *ACS Appl. Mater. Interfaces*, 2011, **3**, 4165-4168.
13 S. A. Webb, C. A. Bridges and G. M. Veith, *J. Power Sources*, 2014, **248**, 1105-1117.
14 H. Lu, L. Wu, L. Xiao, X. Ai, H. Yang and Y. Cao, *Electrochim. Acta*, 2016, **190**, 402-408.
15 B. Zhang, R. Dugas, G. Rousse, P. Rozier, A. M. Abakumov and J.-M. Tarascon, *Nat. Commun.*, 2016, **7**, 1-9.
16 A. Ponrouch, A. Goñi and M. R. Palacín, *Electrochem. Commun.*, 2013, **27**, 85-88.
17 A. Beda, F. Rabuel, M. Morcrette, S. Knopf, P.-L. Taberna, P. Simon and C. Matei Ghimbeu, *J. Mater. Chem. A*, 2021, DOI: 10.1039/D0TA07687B.
18 G. G. Eshetu, T. Diemant, M. Hekmatfar, S. Grugeon, R. J. Behm, S. Laruelle, M. Armand and S. Passerini, *Nano Energy*, 2019, **55**, 327-340.
19 J. Patra, H.-T. Huang, W. Xue, C. Wang, A. S. Helal, J. Li and J.-K. Chang, *Energy Storage Mater.*, 2019, **16**, 146-154.
20 J. Zheng, S. Chen, W. Zhao, J. Song, M. H. Engelhard and J.-G. Zhang, *ACS Energy Lett.*, 2018, **3**, 315-321.
21 J. Lee, Y. Lee, J. Lee, S.-M. Lee, J.-H. Choi, H. Kim, M.-S. Kwon, K. Kang, K. T. Lee and N.-S. Choi, *ACS Appl. Mater. Interfaces*, 2017, **9**, 3723-3732.

 

22 J. Hwang, A. N. Sivasengaran, H. Yang, H. Yamamoto, T. Takeuchi, K. Matsumoto and R. Hagiwara, *ACS Appl. Mater. Interfaces*, 2021, DOI: 10.1021/acsami.0c17807.
23 G. Clark and A. Tai, *Science*, 1948, **107**, 505-505.
24 Y. Fang, J. Zhang, L. Xiao, X. Ai, Y. Cao and H. Yang, *Adv. Sci.*, 2017, **4**, 1600392.
25 J. Qiao, L. Ning, M. S. Molokeev, Y.-C. Chuang, Q. Liu and Z. Xia, *J. Am. Chem. Soc.*, 2018, **140**, 9730-9736.
26 Y.-X. Ma, Y.-P. Gong, C.-l. Hu, J.-G. Mao and F. Kong, *J. Solid State Chem.*, 2018, **262**, 320-326.
27 D. Schildhammer, G. Fuhrmann, L. L. Petschnig, K. Wurst, D. Vitzthum, M. Seibald, H. Schottenberger and H. Huppertz, *Inorg. Chem.*, 2017, **56**, 2736-2741.
28 H. Yu, W. Zhang, J. Young, J. M. Rondinelli and P. S. Halasyamani, *Adv. Mater.*, 2015, **27**, 7380-7385.
29 A. Choudhury, S. Natarajan and C. N. R. Rao, *Chem. Commun.*, 1999, 1305-1306.
30 P. H. Abelson, *Science*, 1999, **283**, 2015-2016.
31 S. G. Jantz, L. van Wüllen, A. Fischer, E. Libowitzky, E. J. Baran, M. Weil and H. A. Höppe, *Eur. J. Inorg. Chem.*, 2016, **2016**, 1121-1128.
32 K. Tasaki, K. Kanda, S. Nakamura and M. Ue, *J. Electrochem. Soc.*, 2003, **150**, A1628-A1636.
33 K. Matsumoto and R. Hagiwara, *Inorg. Chem.*, 2009, **48**, 7350-7358.
34 A. V. Plakhotnyk, L. Ernst and R. Schmutzler, *J. Fluorine Chem.*, 2005, **126**, 27-31.
35 R. Fernández-Galán, B. R. Manzano and A. Otero, *J. Organomet. Chem.*, 1999, **577**, 271-282.
36 C. Wang, L. Yu, W. Fan, J. Liu, L. Ouyang, L. Yang and M. Zhu, *ACS Appl. Energy Mater.*, 2018, **1**, 2647-2656.
37 C. Wang, L. Yu, W. Fan, R. Liu, J. Liu, L. Ouyang, L. Yang and M. Zhu, *J. Alloys Compd.*, 2018, **755**, 1-9.
38 K.-E. Kim, J. Y. Jang, I. Park, M.-H. Woo, M.-H. Jeong, W. C. Shin, M. Ue and N.-S. Choi, *Electrochem. Commun.*, 2015, **61**, 121-124.
39 Y.-M. Song, C.-K. Kim, K.-E. Kim, S. Y. Hong and N.-S. Choi, *J. Power Sources*, 2016, **302**, 22-30.
40 B. Yang, H. Zhang, L. Yu, W. Fan and D. Huang, *Electrochim. Acta*, 2016, **221**, 107-114.
41 G. Yang, J. Shi, C. Shen, S. Wang, L. Xia, H. Hu, H. Luo, Y. Xia and Z. Liu, *RSC Adv.*, 2017, **7**, 26052-26059.
42 H. Yang, C.-Y. Chen, J. Hwang, K. Kubota, K. Matsumoto and R. Hagiwara, *ACS Appl. Mater. Interfaces*, 2020, **12**, 36168−36176.
43 T. Yang, H. Zeng, W. Wang, X. Zhao, W. Fan, C. Wang, X. Zuo, R. Zeng and J. Nan, *J. Mater. Chem. A*, 2019, **7**, 8292-8301.
44 D. D. DesMarteau, P. A. Bernstein, F. A. Hohorst and M. Eisenberg, *Inorg. Chem.*, 1971, **10**, 1549-1551.
45 R. C. Thompson and W. Reed, *Inorg. Nucl. Chem. Lett.*, 1969, **5**, 581-585.
46 G. Han, Y. Wang, H. Li, Z. Yang and S. Pan, *Chem. Commun.*, 2019, **55**, 1817-1820.
47 R. W. Harrison, R. C. Thompson and J. Trotter, *J. Chem. Soc.*, 1966, 1775-1780.
48 W. Granier, J. Durand, L. Cot and J. Galigne, *Acta. Cryst. B*, 1975, **31**, 2506-2507.
49 J. Trotter and S. Whitlow, *J. Chem. Soc. A*, 1967, 1383-1386.
50 R. Harrison and J. Trotter, *J. Chem. Soc. A*, 1969, 1783-1787.
51 P. J. Malinowski, D. Kurzydłowski and W. J. D. T. Grochala, *Dalton Trans.*, 2015, **44**, 19478-19486.
52 A. Altomare, G. Cascarano, C. Giacovazzo and A. Guagliardi, *J. Appl. Crystallogr.*, 1993, **26**, 343-350.
53 G. Sheldrick, *Acta Cryst. A*, 2015, **71**, 3-8.
54 L. J. Farrugia, *J. Appl. Crystallogr.*, 1999, **32**, 837-838.
55 K. Bühler and W. Bues, *Z. Anorg. Allg. Chem.*, 1961, **308**, 62-71.
56 R. J. Gillespie and P. L. A. Popelier, *Chemical Bonding and Molecular Geometry*, Oxford University Press, New York, 2001.
57 I. H. R. J. Gillespie, *The VSEPR Model of Molecular Geometry*, Allyn and Bacon, Boston, 1991.
58 M. Weil, M. Puchberger, E. Füglein, E. J. Baran, J. Vannahme, H. J. Jakobsen and J. Skibsted, *Inorg. Chem.*, 2007, **46**, 801-808.
59 D. Iermakova, R. Dugas, M. Palacín and A. Ponrouch, *J. Electrochem. Soc.*, 2015, **162**, A7060-A7066.
60 M. Forsyth, H. Yoon, F. Chen, H. Zhu, D. R. MacFarlane, M. Armand and P. C. Howlett, *J. Phys. Chem. C*, 2016, **120**, 4276-4286.
61 J. Hwang, K. Matsumoto and R. Hagiwara, *J. Phys. Chem. C*, 2018, **122**, 26857−26864.
62 K.-H. Chen, K. N. Wood, E. Kazyak, W. S. LePage, A. L. Davis, A. J. Sanchez and N. P. Dasgupta, *J Mater Chem A*, 2017, **5**, 11671-11681.
63 S. Komaba, W. Murata, T. Ishikawa, N. Yabuuchi, T. Ozeki, T. Nakayama, A. Ogata, K. Gotoh and K. Fujiwara, *Adv. Funct. Mater.*, 2011, **21**, 3859-3867.
64 M. Dahbi, T. Nakano, N. Yabuuchi, T. Ishikawa, K. Kubota, M. Fukunishi, S. Shibahara, J.-Y. Son, Y.-T. Cui and H. Oji, *Electrochem. Commun.*, 2014, **44**, 66-69.
65 R. Petibon, C. P. Aiken, N. N. Sinha, J. C. Burns, H. Ye, C. M. VanElzen, G. Jain, S. Trussler and J. R. Dahn, *J. Electrochem. Soc.*, 2012, **160**, A117-A124.
66 N. Ogihara, S. Kawauchi, C. Okuda, Y. Itou, Y. Takeuchi and Y. Ukyo, *J. Electrochem. Soc.*, 2012, **159**, A1034-A1039.
67 D. Andre, M. Meiler, K. Steiner, C. Wimmer, T. Soczka-Guth and D. Sauer, *J. Power Sources*, 2011, **196**, 5334-5341.
68 F. Wohde, M. Balabajew and B. Roling, *J. Electrochem. Soc.*, 2016, **163**, A714.
69 R. Alcantara, M. Jaraba, P. Lavela and J. Tirado, *J. Electroanal. Chem.*, 2004, **566**, 187-192.
70 F. Croce, F. Nobili, A. Deptula, W. Lada, R. Tossici, A. D'epifanio, B. Scrosati and R. Marassi, *Electrochem. Commun.*, 1999, **1**, 605-608.
71 C. Fleischer, W. Waag, H.-M. Heyn and D. U. Sauer, *J. Power Sources*, 2014, **260**, 276-291.
72 J. Gomez, R. Nelson, E. E. Kalu, M. H. Weatherspoon and J. P. Zheng, *J. Power Sources*, 2011, **196**, 4826-4831.
73 W. Cao, J. Zheng, D. Adams, T. Doung and J. P. Zheng, *J. Electrochem. Soc.*, 2014, **161**, A2087.
74 Y. Pan, Y. Zhang, B. S. Parimalam, C. C. Nguyen, G. Wang and B. L. Lucht, *J. Electroanal. Chem.*, 2017, **799**, 181-186.
75 D.-H. Kim, B. Kang and H. Lee, *J. Power Sources*, 2019, **423**, 137-143.
76 K. Pan, H. Lu, F. Zhong, X. Ai, H. Yang and Y. Cao, *ACS Appl. Mater. Interfaces*, 2018, **10**, 39651-39660.
77 J. Song, B. Xiao, Y. Lin, K. Xu and X. Li, *Adv. Energy Mater.*, 2018, **8**, 1703082.

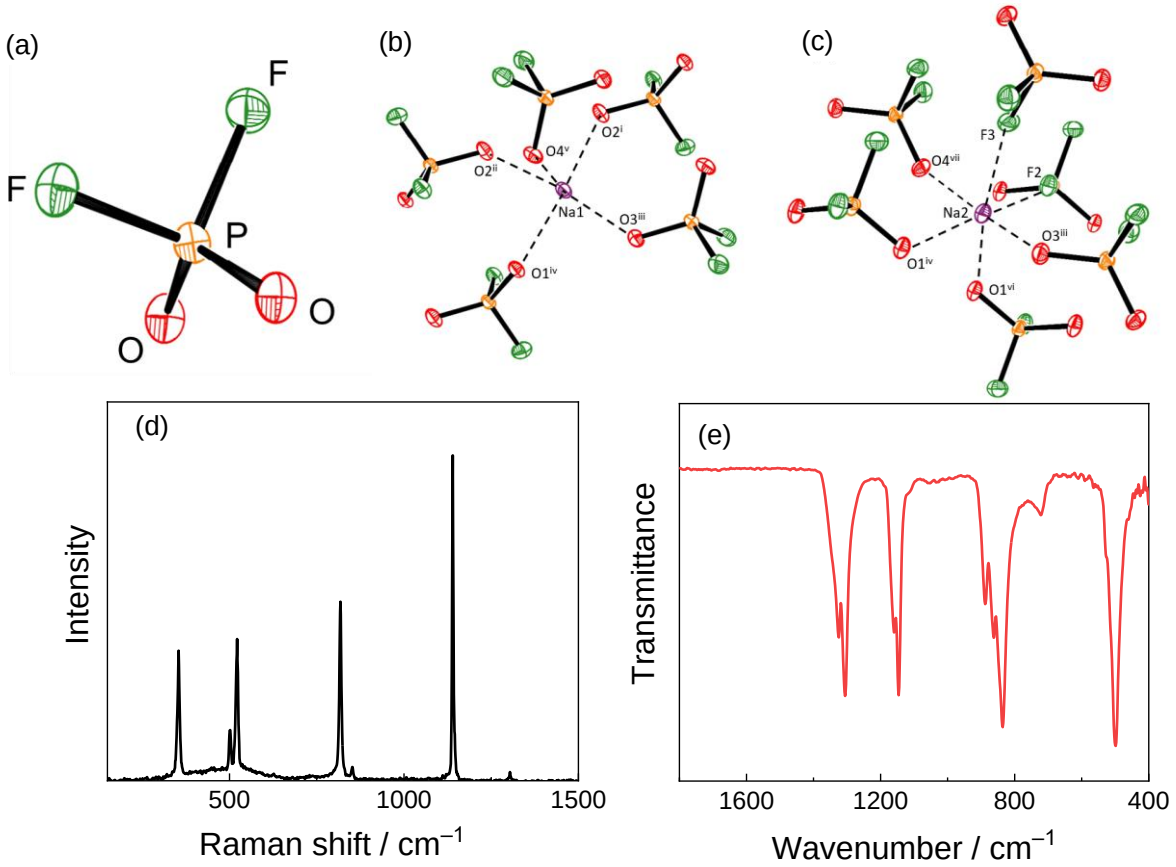


**Fig. 1** (a) Molecular structure of $DFP^-$ in NaDFP determined at 113 K. Coordination environments of (b) Na1 and (c) Na2 in NaDFP [symmetry code: (i) x+1, y−1, z; (ii) −x+2, −y, −z+2; (iii) −x+2, −y, −z+2; (iv) x+1, y, z; (v) x, y−1, z+1; (vi) −x+1, −y, −z+2; (vii) −x+2, −y+1, −z+1]. Thermal ellipsoids are shown at the 50 % probability level. (d) Raman and (e) IR spectra of NaDFP.

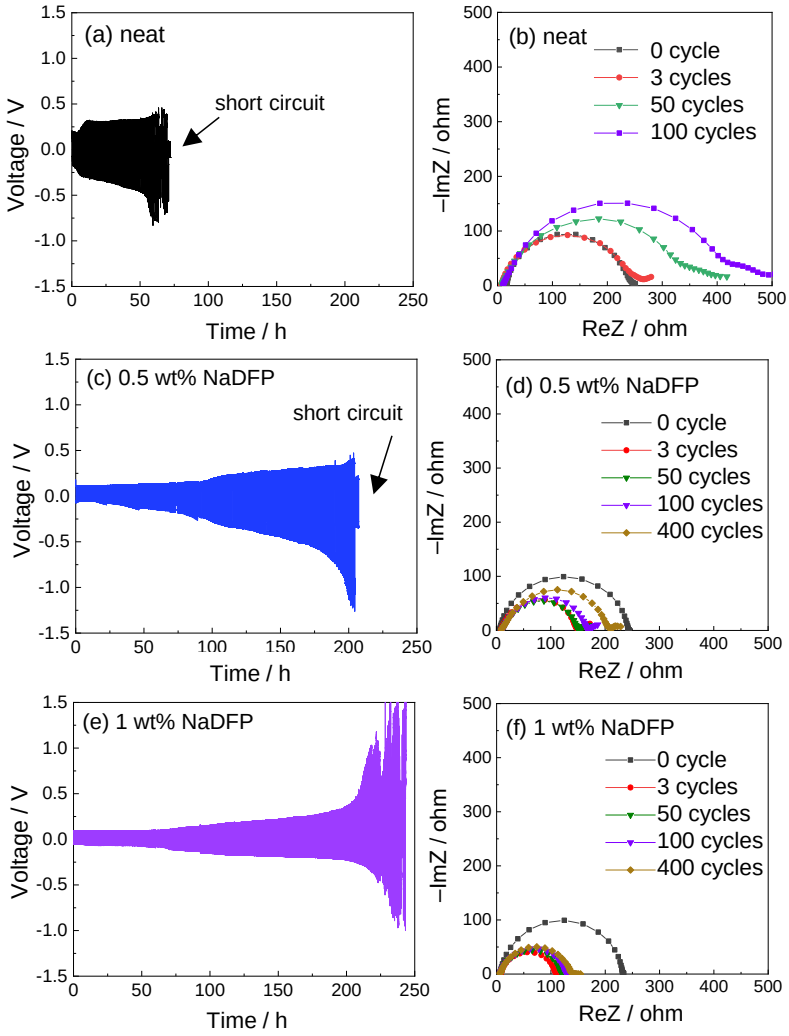


**Fig. 2** Voltage profiles and Nyquist plots of the Na/Na symmetrical cells during galvanostatic Na metal deposition/dissolution cycles using 1 M $NaPF_6$-EC/DMC (1:1, v:v) electrolute with (a, b) 0 wt% NaDFP (neat), (c, d) 0.5 wt% NaDFP and (e, f) 1 wt% NaDFP. Current density: 1 mA $cm^{-2}$. (See Fig. S6 in ESI† for voltage profiles and Nyquist plots with 0.5 wt% FEC and 3 wt% FEC)

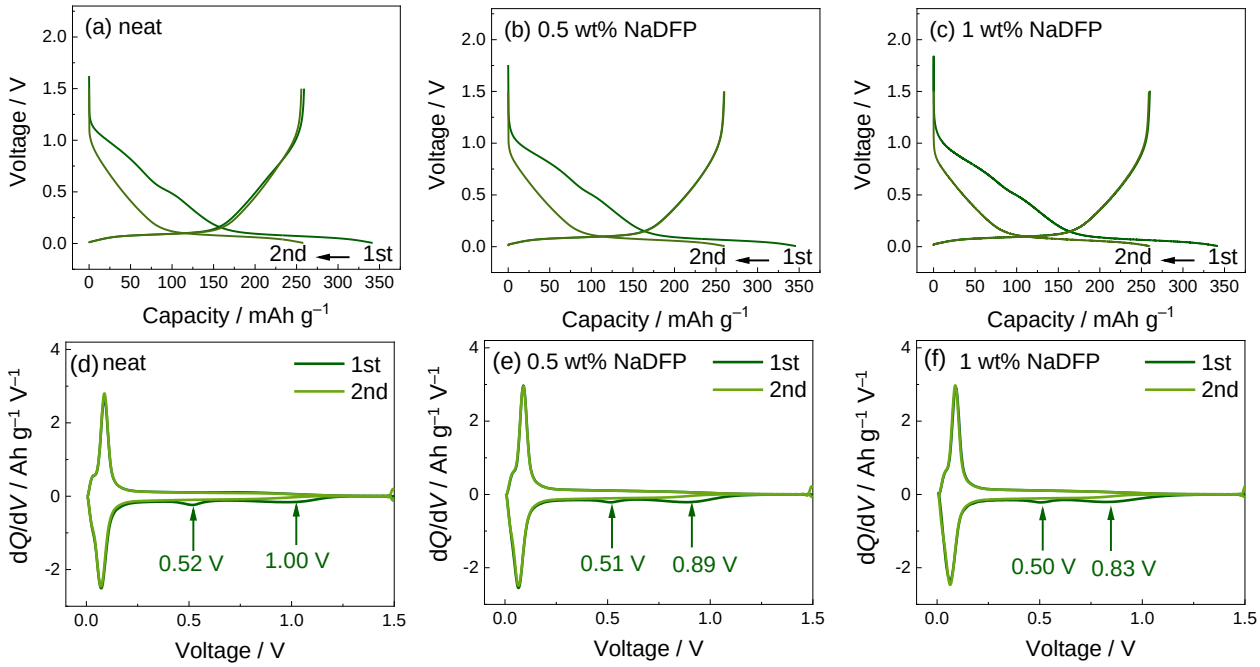


Fig. 3 Charge-discharge curves and the corresponding differential capacity-voltage (d*Q*/d*V)* plots of the Na/HC cells using 1 M $NaPF_6$-EC/DMC (1:1, v:v) electrolyte with (a, d) 0 wt% NaDFP (neat), (b, e) 0.5 wt% NaDFP and (c,f) 1 wt% NaDFP. Current density: 25 mA $g^{-1}$. Cut-off voltage: 0.005–1.5 V. (See Fig. S7 in ESI† for the data with 0.5 wt% FEC and 3 wt% FEC .

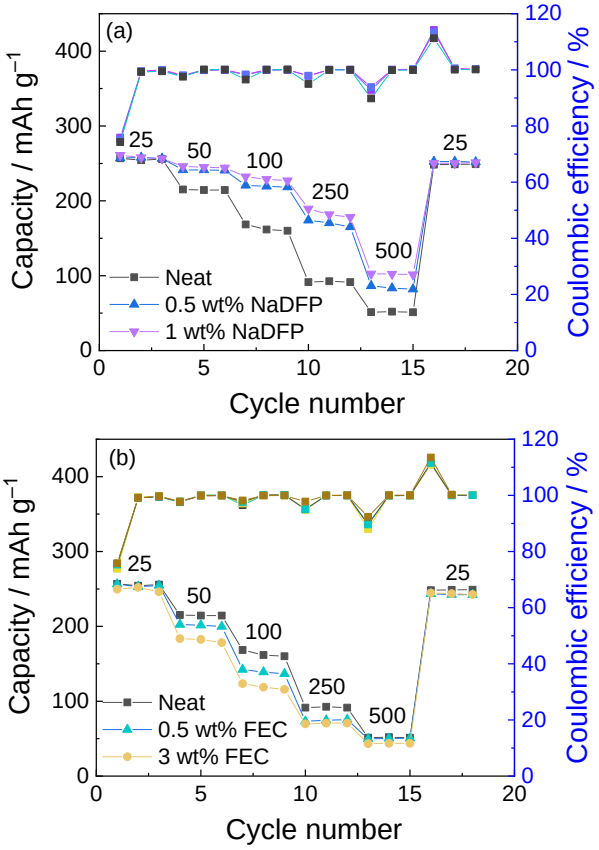


**Fig. 4** Rate capability of the Na/HC cells using 1 M $NaPF_6$-EC/DMC (1:1, v:v) electrolyte with (a) 0 wt% NaDFP (neat), 0.5 wt% NaDFP and 1 wt% NaDFP and (b) 0 wt% FEC (neat), 0.5 wt% FEC and 3 wt% FEC. Cut-off voltage: 0.005–1.5 V. Electrolytes: Current densities are shown in mA $g^{-1}$.

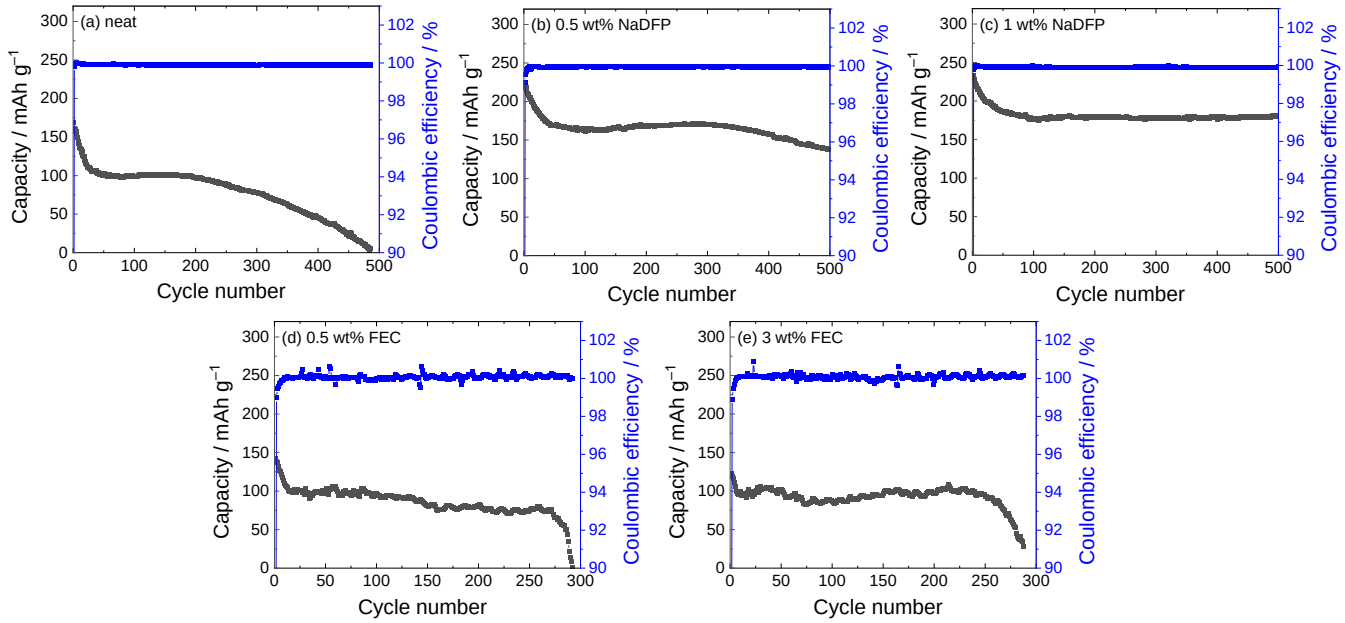


**Fig. 5** Cycle performance of the Na/HC cells using 1 M $NaPF_6$-EC/DMC (1:1, v:v) electrolyte with (a) 0 wt% NaDFP (neat), (b) 0.5 wt% NaDFP, (c) 1 wt% NaDFP, (d) 0.5 wt% FEC, and (e) 3 wt% FEC. Current density: 100 mA g$^{-1}$. Cut-off voltage: 0.005–1.5 V. (See Fig. S8 in ESI† for the corresponding Charge-discharge curves and d*Q*/d*V* plots)

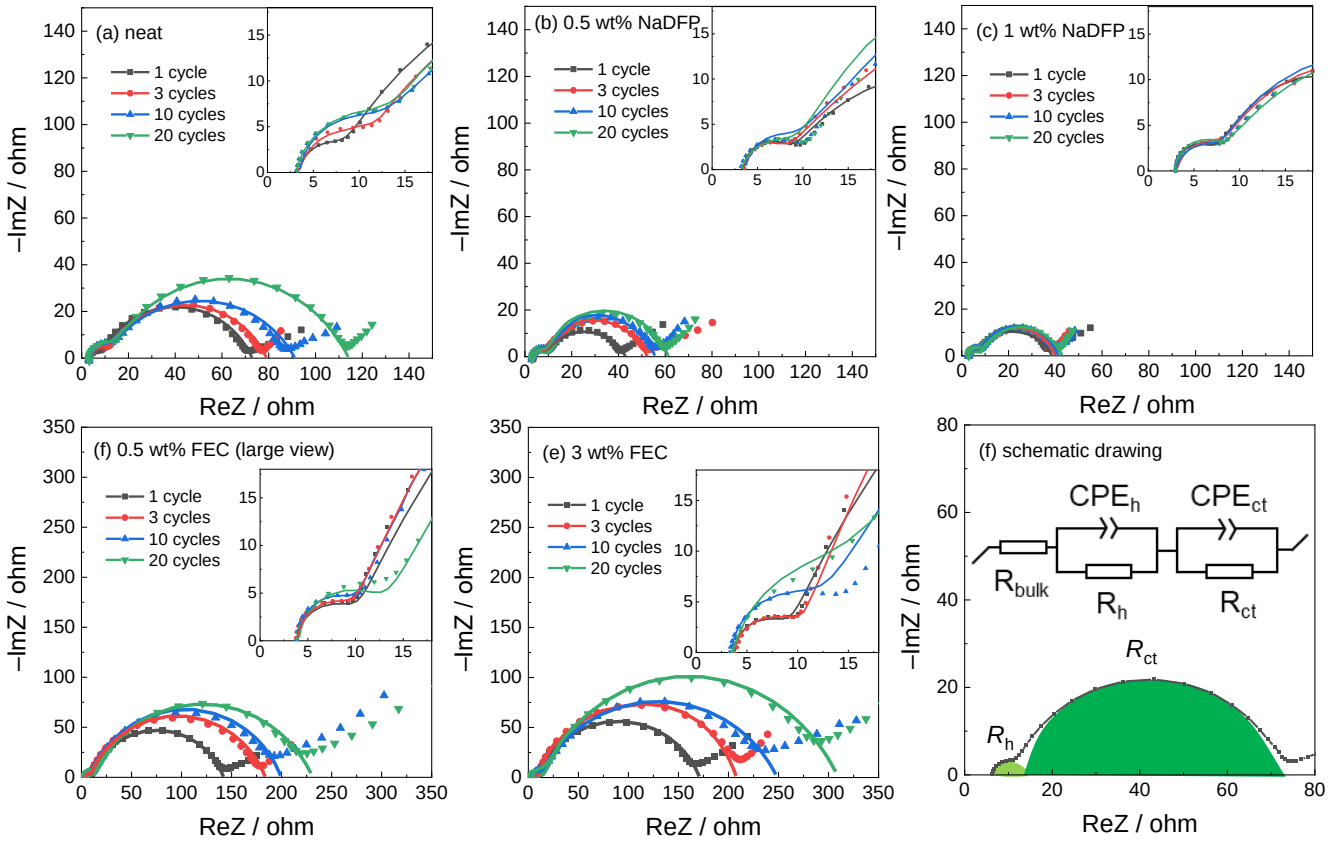


**Fig. 6** Nyquist plots of the HC/HC symmetric cells using 1 M $NaPF_6$-EC/DMC (1:1, v:v) electrolyte with (a) 0 wt% NaDFP (neat), (b) 0.5 wt% NaDFP, (c) 1 wt% NaDFP, (d) 0.5 wt% FEC, and (e) 3 wt% FEC, and (h) the schematic drawing of the fitting parameters for the arc. Frequency range of 100 kHz–10 mHz. AC amplitude: 10 mV. See Table S7 in ESI† EIS parameters)

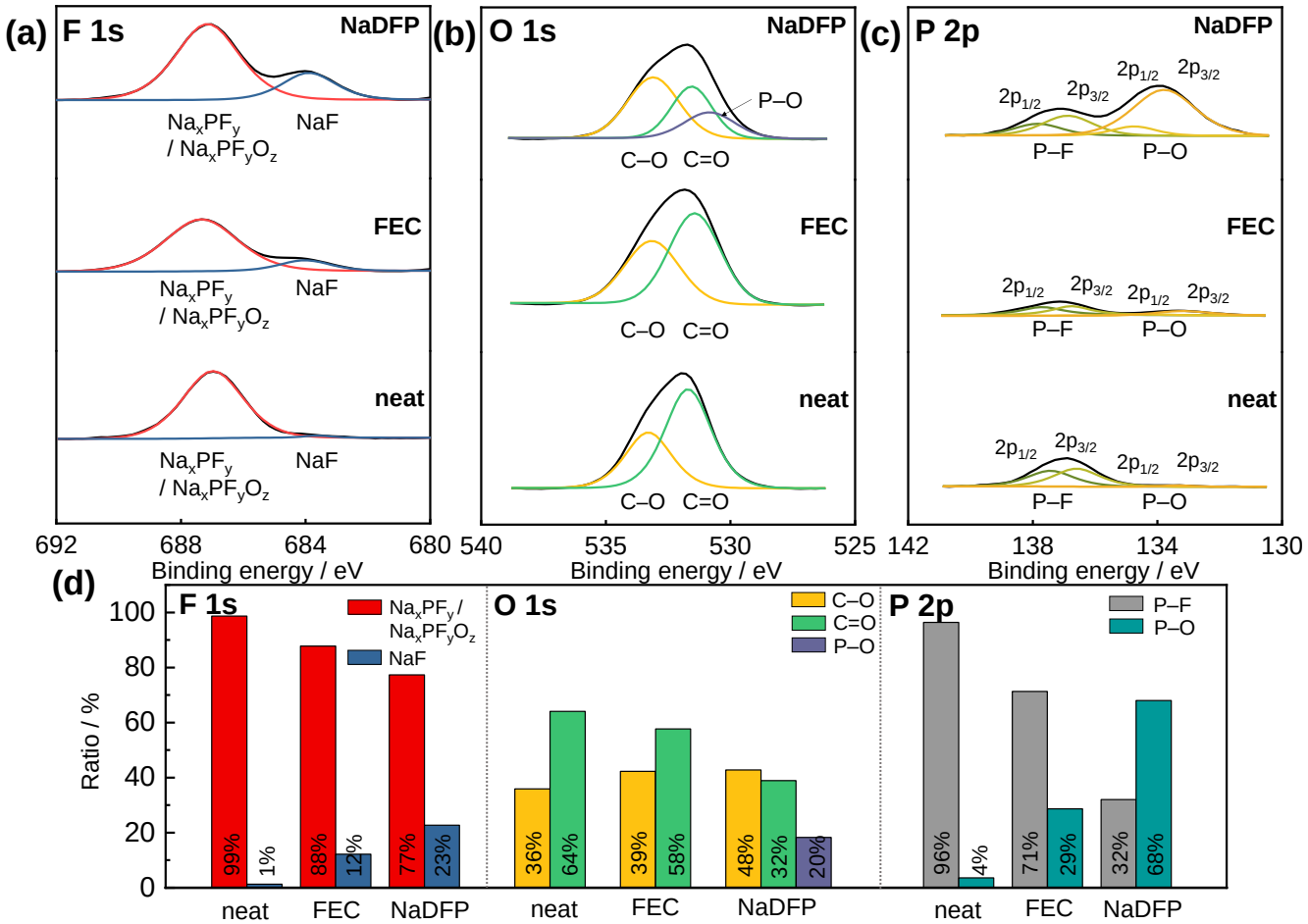


**Fig. 7** X-ray photoelectron spectra of the SEI layers formed on the HC electrodes after 20 cycles in 1 M $NaPF_6$-EC/DMC (1:1, v:v) electrolyte with 0 wt% NaDFP (neat), 1 wt% NaDFP and 3 wt% FEC additives in the (a) F 1s, (b) O 1s, and (c) P 2p regions, and (d) SEI component ratios (see Table S8 in ESI† for the binding energy of the peaks).